Research Article | Vol. 27, No. 15 | 22 Jul 2019 | OPTICS EXPRESS 20397
Optics EXPRESS

Cavity-driven hybrid plasmonic ultra-narrow bandpass filter

JINBO GAO,[1,2] JINSONG GAO,[1,2] HAIGUI YANG,[1,*] HAI LIU,[1,4] XIAOYI WANG,[1] KE WANG,[1,2] XIAOYI LIU,[3] QIANG LI,[1] YANCHAO WANG,[1] ZIZHENG LI,[1] RUOQIAN GAO,[1,2] AND ZHUO ZHANG[1]

[1]*Key Laboratory of Optical System Advanced Manufacturing Technology, Changchun Institute of Optics, Fine Mechanics and Physics, Chinese Academy of Sciences, Changchun 130033, China*
[2]*University of the Chinese Academy of Sciences, Beijing 100039, China*
[3]*Université Paris-Est, ESYCOM Lab., ESIEE Paris, Noisy-le-Grand, Paris 93162, France*
[4]*nmliuhai@163.com*
[*]*yanghg@ciomp.ac.cn*

Abstract: We propose a novel compound grating structure that exhibits a tunable ultra-narrowband transmission in the near infrared regime. The thin microstructure can realize a steep wave form through a Fano-like resonance by coupling different propagation-type SPP modes and with a narrow line width formed by the energy band gap. Additionally, the out-of-band suppression is remarkably enhanced. It effectively solves the constraint relationship between high transmittance, narrow line width, and weak side peak of the plasmonic filter, and the structure is suitable for integration with detectors in the near infrared regime.

1. Introduction

Plasmonics is an important branch of nanophotonics with far-reaching significance in modern optics. This branch mainly concerns the interaction of light and matter limited to the wavelength or subwavelength scale of light [1–5]. Nowadays, there is a strong interest in surface plasmon polaritons (SPPs) which is a special electromagnetic wave propagating along the interface between the metal and the medium [6,7]. The optical properties of the plasmonic metasurfaces prepared by this principle depend on the dielectric properties of the materials adopted and the geometry of the system [8–11]. It can optimize the design to independently or simultaneously control the amplitude [12], polarization [13], phase [13,14], and energy of light [15]. The strong localization and high binding of the SPPs make these structures enhance the light field while keeping the thickness much smaller than the operating wavelength [16,17]. Thus the corresponding optical components and systems are easier to miniaturize and integrate. The devices based on SPPs have great application value across broad fields: biochemical sensors [18,19], nanolaser [20,21], waveguide [22,23], plasmonic photocatalysts [24], nonlinear optics [25,26] and energy harvester [27–30].

At the end of the last century, Ebbesen et al. reported a pioneering study on the presence of an extraordinary optical transmission (EOT) through subwavelength hole arrays [31]. This experiment converted the incident light through the periodic modulation of holes into SPPs at the interface of the opaque metal film. The subsequent reverse conversion of the excited SPPs into outgoing photons caused anomalous effects of the observed reflection and transmission. This method broke the limitations of traditional optical films for light field control and maintained the excellent properties of miniaturization, easy integration and precise modulation. The related filters prepared using this concept had the attractive characteristics of low cost, miniaturization, and tunability. Although the addition of metals leads to losses in the transmission efficiency of the structures, some effective solutions have been proposed [32,33]. For a single aluminum layer filter of a triangular circular hole lattice regularly arranged on glass, the transmittance obtained in the visible spectrum is between 30% and

#364181 https://doi.org/10.1364/OE.27.020397
Journal © 2019 Received 3 Apr 2019; revised 14 Jun 2019; accepted 20 Jun 2019; published 9 Jul 2019

Optics EXPRESS

35%; the corresponding line width is greater than 100 nm [34]. Plasmonic Fabry-Perot (FP) metal-insulator-metal (MIM) stack arrays were observed to increase the transmittance to 60% with a line width of 110 nm in the visible region [35]. The line width ($\Delta\lambda$) refers to the bandwidth of the transmission spectrum, which corresponds to full width at the half maximum (FWHM). Recently, Shah et al. designed a subwavelength asymmetric elliptical and circular nanohole array structure, which achieved a line width of 79 nm and transmittance of 44% in the near infrared regime. To the best of our knowledge this is also the narrowest line width of plasmonic filters in the near-infrared ever reported based on the principle of SPPs [36]. However, it has been proved that even narrower-bandpass plasmonic filters, with the high transmittance strongly required in some practical applications, are still difficult to achieve. In addition, poor out-of-band suppression also causes unnecessary side peaks to be observed in the vicinity of the transmission main peak. Therefore, a high-performance plasmonic filter with a narrower line width based on SPPs is still an extremely great challenge.

In this study, we propose a novel non-porous composite grating array with anomalous transmission by using the coupling of different propagation-type SPPs. In order to better demonstrate the optical properties of the compound-grating system, we define the quality factor $Q = \lambda_c/\Delta\lambda$, where the λ_c is the center wavelength of the passband. The design eventually exhibits an extremely narrow line width (at the level of 10 nm) and high Q (>100) with the transmittance of nearly 35% in the near-infrared (1.4-1.7 μm) window. Furthermore, we can modulate the resonant wavelength and narrow line width of the structure simultaneously, and inhibit the effects of side peaks. Different from traditional SPPs [37,38], coupling of the propagation-type SPPs effectively reduces the constraints between narrow line width and high transmission. The advantages of narrow line width, high transmission, and weak side peaks make the filter we designed suitable for integration with detectors such as gas detection, biosensors, and multi-spectral imaging.

2. Modeling and simulations

The finite difference-time domain (FDTD) method by commercial software (Lumerical FDTD Solutions) was adopted to analyze the characteristics of designed structures. In modeling and simulations, the incident light with a wavelength range from 900 nm to 2200 nm propagates along the negative z-direction with the electric field polarization in the x-direction. The stripes of the simulation structrue are periodically arranged in the x-direction and infinitely extended in the y-direction. The asymmetric and symmetric boundary conditions were used in the x- and y-directions, respectively, under normal incidence to form the unit cells based on the symmetry of the model. The perfectly matched layers condition was adopted in the z direction. The characteristic parameters for the gold (Au) and silicon dioxide (SiO_2) such as the permittivity and refractive index were obtained from the Palik database. To guarantee the accuracy and convergence of the simulation, we adopted the high accuracy with the size of 5 nm × 5 nm × 5 nm and a series of repeated calculations.

3. Discussion and results

It is well known that the propagating wavenumber k_{spp} of SPPs is larger than that light in the medium. Under normal incident light, free space radiation is difficult to directly couple to the surface plasmons (SPs), but with the help of the gratings, additional momentum can be used to excite the SPP [39]. Hence, the compound-grating structure we proposed consists of two parts: 1) a series of equally spaced metal-insulator-metal (MIM) gratings, and 2) metal-insulator (MI) gratings with slightly lower height sandwiched between them covering a SiO_2 substrate, as illustrated in Fig. 1. These two parts are used to provide coupling of different SPP modes with each other to create a unique transmission phenomenon. The widths of MIM and MI gratings are set to W_1 and W_2, respectively. The thickness of the top gold film denoted as h_2 and the SiO_2 layer denoted as H of two sections are the same. According to the

Optics EXPRESS

structural constraint, the height difference between the two types of stripes is the thickness of the Au film denoted as h_1 which is the bottom layer of the MIM gratings. Unless otherwise stated, the values of h_1, h_2, and H are set to be 50 nm, 25 nm, and 140 nm, respectively. The origin of these dimensions of the initial structure will be revealed later.

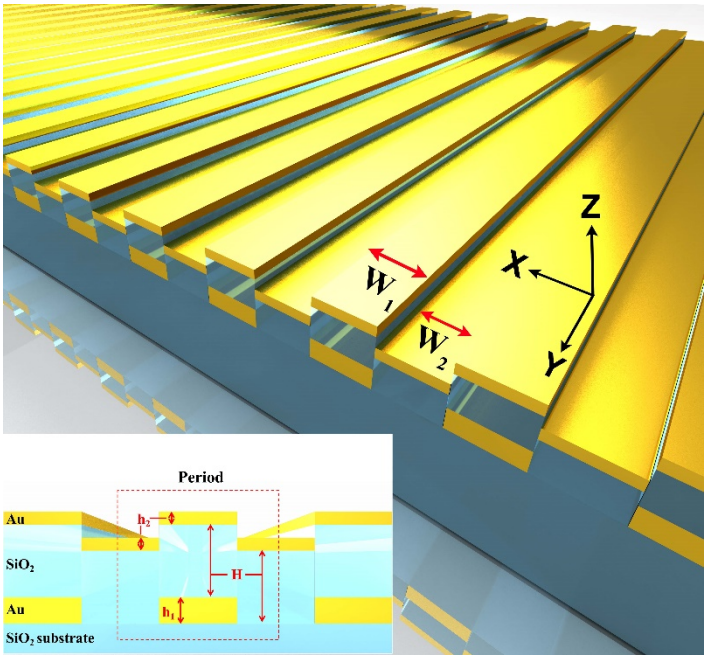

Fig. 1. Diagram of the designed compound-grating microstructure. The inset shows the structural details of the hybrid gratings. The materials of the gold region (metal layer) and the transparent blue region (dielectric spacer and substrate) are used as Au and SiO_2, respectively.

The inherent short-lifetime characteristics of SPs create a broadband resonance spectrum due to the effects of damped electron oscillations [32]. To realize the narrowband response of SPs, the higher-order plasmon resonance coupling forms an effective route to reduce the resonance bandwidth [40]. When the compound-grating period (P) is greater than 1.7 μm, there will only be the intrinsic higher order SP resonance in the target spectral range (1.4-1.7 μm). This is because the resonant wavelength of the fundamental mode exceeds P at normal incidence. When the P is 2 μm and the width ratio is W_2: W_1 = 1:1, there is a transmission mode of the ultra-narrow peak (A mode), as shown in Fig. 2(a). Its center wavelength is 1.45 μm where the transmissivity is 49.6%, and the Q is as high as 96.8 with an ultra-narrow FWHM of only 15 nm. It should be pointed out that it is generally difficult to maintain this level of transmission through the tens of nanometers of the non-porous gold layer in the near-infrared regime. This interesting transmission phenomenon is attributed to a single Au-SiO_2 interface SPP (S_{spp}) excited by the wave vector increment provided by the grating coupling and the plasmonic resonant cavity. Its magnetic and electric field distributions illustrated in Figs. 2(b) and 2(c) exhibits a stable mode and apparent propagation characteristics along the surface. We can express and prove this optical property by the following theory [41,42]:

$$k_{\text{mode}} = k_0 \sin\theta + iG \tag{1}$$

$$k_{sp} = k_0 \sqrt{\frac{\varepsilon_m \varepsilon_d}{\varepsilon_m + \varepsilon_d}} \tag{2}$$

Optics EXPRESS

Equation (1) is the Bragg coupling condition for the gratings, in which $k_0 = w/c$ is the wave vector of the incident light, integer i is the diffraction order of grating for the reciprocal lattice vector G ($G = 2\pi/P$), and θ is the incidence angle from free space. Equation (2) indicates the wave vector of the SPs; ε_m and ε_d are the dielectric constants of the metal and insulator medium respectively. The permittivity of Au and SiO_2 used in the simulation are extracted from the data of Palik [43]. Only when $k_{mode} = k_{sp}$ does light couple to SPs, the electromagnetic energy is then captured on the surface immediately, raising the transmission peak [7].

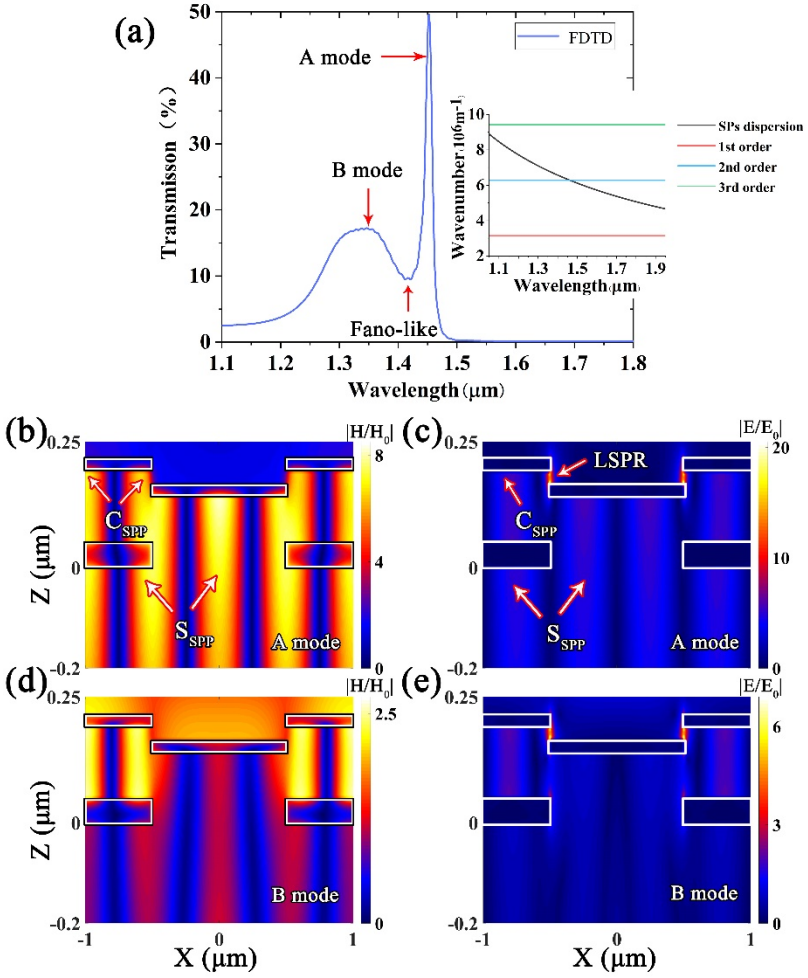

Fig. 2. (a) Simulated transmission spectrum from the design exhibits high transmission, ultra narrow line width, and the resonance position of the two hybrid modes. The inset indicates the dispersion relation of SPs and different Bragg coupling orders. (b) and (c) Longitudinal relative magnetic-field and electric-field intensity distributions of the microstructure of A mode resonance respectively. (d) and (e) Longitudinal relative magnetic and electric field distributions of B mode resonance respectively. The color bars stand for the normalized field intensity.

The inset in Fig. 2(a) is the dispersion relationship of SPs and Bragg coupling orders. The black line is the wave vector threshold condition required to excite the SPs on the interface between Au and SiO_2, other color lines correspond to different orders of Bragg coupling conditions under TM normal incidence. The two types of modes match and excite the S_{spp} at the wavelength of 1.462 μm, which coincides well with the ultra-narrow peak position in Fig.

Optics EXPRESS

2(a). In this case, the wave number of S_{spp} is $k_{spp} = 6.28*10^6 + 2.50*10^3 i$, and the theoretical wavelength $\lambda_{spp}(2\pi/\mathrm{Re}(k_{spp}))$ is 1 μm, corresponding to four main orders of standing waves under the condition of P = 2 μm. This energy distribution is consistent with the optical properties of the electric and magnetic fields in Figs. 2(b) and 2(c). It also explains why the Au-SiO_2 interfaces underneath the surface of Au layer in the MI grating and the bottom of the MIM can simultaneously generate a stable SPP: In this resonance mode, the S_{spp} receives momentum from cavity SPP (C_{spp}) formed in the MIM transverse Fabry-Perot (FP) cavity, and it obtains initial energy and the additional supplement from the Bragg coupling momentum. The excited S_{spp} have both the transverse wave vector kx and the vertical wave vector kz. These two metal layers are not continuous; however, the height difference of 140 nm is much smaller than the SPP penetration depths of 1.06 μm extracted by the relation $L_d = k_0^{-1} | (\varepsilon_m + \varepsilon_d) / \varepsilon_d^2 |^{1/2}$ in dielectric [12]. Therefore, SPs and light are not decoupled and still transmitted in the form of SPP, which looks like the S_{spp} mode "jumps" across the surface underneath the two gold layers. In order to prevent SPPs in the compound-grating system from passing through the top gold layers to exchange energy with the outside, and avoid the interference from the external environment, and using the relation $L_m = k_0^{-1} | (\varepsilon_m + \varepsilon_d) / \varepsilon_m^2 |^{1/2}$ [12], we calculated the maximum penetration depths in the working wavelength range of the SPPs produced at the Au-SiO_2 and Au-air interfaces to be 24.1 nm and 24.3 nm, respectively. Therefore, when h_2 is adopted as 25 nm, the resonance mode of S_{spp} and C_{spp} will not be affected by external factors.

In fact the coupling of S_{spp} and C_{spp} in the transmission spectrum of the compound-grating system has always existed, but there is an energy difference between the two types of SPPs. When S_{spp} occupies a larger proportion of energy, the A mode is the coupled state corresponding to the peak frequency of the transmission spectrum. In contrast when C_{spp} has the energy advantage, the coupled state at the peak frequency is called the B mode. The electric and magnetic fields of the B mode at the peak wavelength of 1.33 μm as shown in Figs. 2(d) and 2(e). As the wavelength of the incident light increases, the electric resonance and magnetic resonance of the C_{spp} in the MIM cavity alternate in different orders. Momentum overflows from the MIM cavity and flows to the lower surface of the two gold layers of the MIM bottom and MI gratings. Since there is a weak resonance intensity of C_{spp} itself, it cannot provide a stable and strong mode at the two Au-SiO_2 interfaces mentioned above, and the energy of transmission is relatively low. The S_{spp} that is driven by compound gratings and the SPP resonant cavity of the A mode is stable and discrete; however, the C_{spp} of B mode is a relatively long conversion process. The Fano resonance generally arises from the constructive and destructive interference of a narrow discrete resonance with a broad spectral line or continuum [45,46]. With the mutual coupling of these two forms of energy, the C_{spp} with the broad bandwidth can interfere destructively with the narrow S_{spp} resonance and eventually produce a distinct asymmetric Fano-type resonance. It shows a similar mechanism to the reported Fano lineshape exhibited by nanowires deposited on slab [46]. A detailed explanation will be given later when we will clarify the formation mechanism of the ultra-narrow line width.

Optics EXPRESS

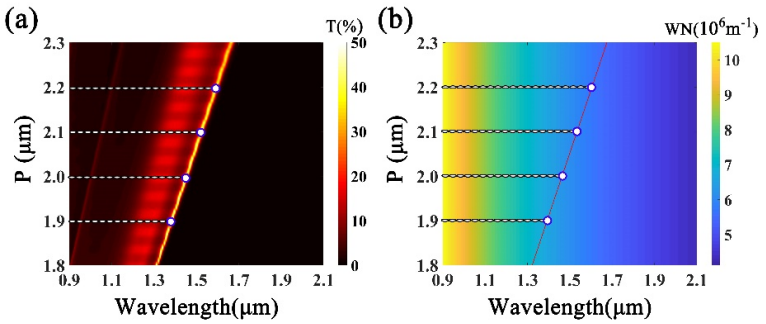

Fig. 3. The ultra-narrow transmission peak for the compound-grating microstructure as a function of wavelength and the period P. (a) The transmission peak wavelength obtained by FDTD simulation; the color bar denotes the transmittance affected by period and wavelength. (b) The resonance position of S_{spp} solved by the mathematical analysis of the dispersion relation; the color bar denotes the wavenumber (WN) of SPs that can be excited under periodic and wavelength conditions.

In order to verify our theory, we have self-certified by the following method. According to Eqs. (1) and (2), we can express the resonance wavelengths of S_{spp} as Eq. (3):

$$\lambda_s = \frac{P}{i}\sqrt{\frac{\varepsilon_m \varepsilon_d}{\varepsilon_m + \varepsilon_d}} \tag{3}$$

It can be observed from Eq. (3) that the resonant wavelength exhibits a period-sensitive optical characteristic. Under the premise of keeping other parameters constant and ensuring the width of W_1 is equal to W_2, we scanned the P from 1.8 to 2.3 μm. Figure 3(a) depicts the simulated period-modulated transmission spectrum of the structure by FDTD. Evidently, the resonance wavelength λ_s with the redshift phenomenon is basically proportional to the increased period of the structure, which is understandable in that it can be naturally obtained by Eq. (3). As the peak frequencies are modulated, transmission spectra with different periods also maintain narrow line widths, which is in line with our expectations. Furthermore, we theoretically calculate the conditions for the match between the SPs dispersion and the second order of Bragg diffraction in different period values. The details are shown in Fig. 3(b). The color bar represents the wave vector space corresponding to the SPs excitation threshold, and the red line is the analytical solution of the theoretical peak λ_s. Obviously, the simulation and calculation results are extremely consistent according to the trend and the peak position, which proves the accuracy and rationality of our theory. The slight discrepancy is due to the coupling effect of the B mode.

In addition we found that when the electric field or magnetic field of C_{spp} is in the integer order, the outer edges of the metal layer at a suitable distance will produce the localized surface plasmon resonance (LSPR) phenomenon, as shown in Fig. 2(c). The localized electric field is further concentrated and magnified through the FP resonance induced by transverse C_{spp}. A similar effect was found in a reported three-layer FP/SPP aluminum absorber [44], but we obtained a higher field magnification at the resonant wavelength. For instance, the remarkable electric field energy enhancement of the A mode is 415.5 times ($|E_{LSPR}/E_0|$ = 20.52), which is far higher than that of previously reported value of 86.5. Considering that LSPR has strong field-enhanced characteristics and its localization at the entrance where light enters the compound gratings, we speculate that LSPR may have the ability to help the system capture more light energy and limit energy dissipation to the outside. The intensity of LSPR should be related to the thickness (h_1-h_2) of the gap between the top layers of the MI and MIM structure, and h_2 has been set to 25 nm in the previous section. For this reason we studied the relationship between the relative energy enhancement of LSPR and the peak transmittance of the A mode as a function of h_1 as shown in Fig. 4(a). The results show that

Optics EXPRESS

the energy enhancement of LSPR decreases with the increase of h_1, but an unexpected result is that the transmittance is not positively correlated with the intensity of LSPR, and the trend is even opposite in the progress of h_1 from 30 to 50 nm. To explore the reason, we show the relative electric field distributions in Fig. 4(b) of the microstructure when h_1 is 30, 40, and 50 nm, respectively. Since the field enhancement of LSPR is too strong, we have down-regulated the upper limit of the color bar to $|E/E_0| = 6$ to facilitate seeing the details of other lower-energy field distributions. Obviously, the stronger LSPR does enhance the resonance of C_{spp} and even produces an energy gain to S_{spp} on the lower surface of the MI metal layer, indicating that LSPR has a positive effect on transmittance. However, when the dimension of h_1 is small as $h_1 = 30$ nm, $LSPR_2$ appears at the edges of the gold layer at the bottom of the MIM structure, which seriously hinders the momentum transfer between the S_{spp} of MI and the S_{spp} of the MIM structure, and it absorbs the energy, resulting in a low total transmittance of the structure. Since LSPR and $LSPR_2$ are intrinsic plasmon resonance modes, both are quite sensitive to the dimensions and shape of the microstructure. As h_1 increases, the energy of both LSPR and $LSPR_2$ decrease. When $h_1 = 50$ nm, the transmittance reaches the extreme value because of the disappearance of the negative influence of $LSPR_2$. After this, the energy of the LSPR continues to weaken, and the transmittance decreases. Therefore, it is reasonable to set h_1 to 50 nm, which not only keeps the structure at a relatively high transmittance, but also eliminates the influence of $LSPR_2$ on S_{spp}.

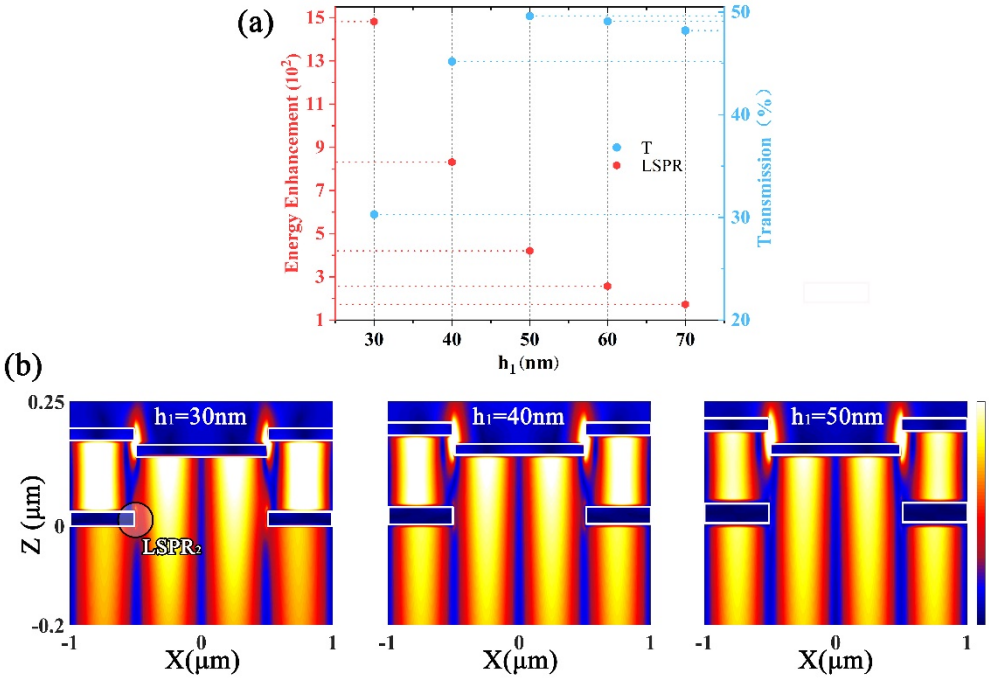

Fig. 4. (a) The corresponding values for energy enhancement ($|E_{LSPR}/E_0|^2$) of LSPR and the peak transmittance of the A mode in different h_1. (b) The relative electric-field intensity distributions with different h_1 of 30, 40 and 50 nm, respectively. The color bar stands for the normalized electric field intensity, and its upper limit is set to be $|E/E_0| = 6$.

In some practical applications, an ideal high-resolution filter tends to form a narrow-band single transmission peak without any side peak. Unfortunately, there is often an undesired side peak near the main transmission peak due to the poor out-of-band rejection of SPPs. To solve this problem, we attempted to change the complex propagation constant β of C_{spp} by adjusting the structural parameters of the MIM cavity, thereby regulating the position of the B mode resonance peak wavelength λ_r and optimizing the transmission performance. Based on

Optics EXPRESS

waveguide theory, even though the wavenumbers of MIM β are different from MI, they can be obtained from the following dispersion relation, Eq. (4) [47–49]:

$$\varepsilon_d k_m + \varepsilon_m k_d \tanh(\frac{k_d}{2} H) = 0 \tag{4}$$

where k_d and k_m are defined as $k_d = (\beta^2 - \varepsilon_d k_0^2)^{1/2}$ and $k_m = (\beta^2 - \varepsilon_m k_0^2)^{1/2}$, other symbols have meanings as before. Using the result from Eq. (4), we can modulate the optical properties of the B mode by changing the thickness of the MIM dielectric layer. Assuming that the two widths of W_1 and W_2 were the same, we swept the thickness of the SiO_2 layer from 70 nm to 210 nm and obtained the corresponding modulated transmission spectrum shown in Fig. 5(a) under the condition that period was P = 2 μm. As H increases, it can be seen from Fig. 5(b) that although the B mode transmission intensity obviously reduces, the main transmission peak of the A mode has almost no attenuation. Notably, the position of the A mode is completely unchanged, as anticipated. This significantly reduces the effects of the transmission side peaks. We additionally give the transmission spectrum of the structure in the absence of the dielectric layer (H = 0 nm). In this case, the unique transmission phenomenon caused by the SPPs disappears completely, leaving only the spectral characteristics of the metallic material in the near-infrared region. It also proves that the SPPs resonance cavity is indispensable for the EOT. However, the ability to adjust the thickness H of the dielectric layer makes it apparently difficult to achieve the separation of the two transmission modes, thus forming a single-peak response. A too thick cavity height will increase the longitudinal dimension of the structure, which is harmful to miniaturization and integration of the device. Using the above regulatory information, we made a good trade-off between transmission capacity and structural miniaturization, and set the parameter H in the previous structure to 140 nm.

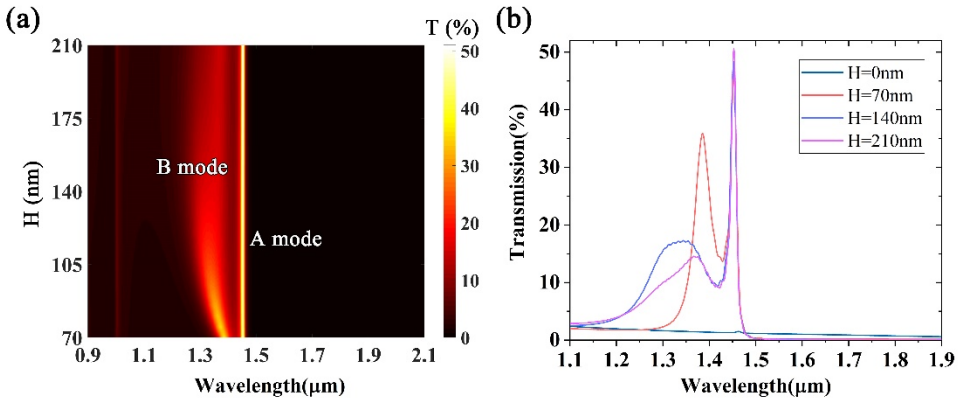

Fig. 5. (a) Side peak intensity suppression of the transmission behavior with varying the thickness H of dielectric layer. The color bar stands for the relative transmittance. (b) Several important characteristic transmission curves are given for specific H values. When the dielectric layer is removed (H = 0 nm), the plasmonic EOT phenomenon will disappear.

Fortunately, we can further carry out large-scale and precise regulation of the B mode, by means of the MIM waveguide resonance conditions given by Eq. (5) [49–51]:

$$2W_1\beta + \phi_r = 2m\pi \tag{5}$$

where ϕ_r is the total phase shift of propagating waves at the left and right facets of the MIM grating, m is the resonance order, and W_1 has the same meaning as above, which actually represents the length of F-P cavity. Therefore, by appropriately adjusting the length of W_1, the resonance order m of C_{spp} and the phase of the facets ϕ_r of A mode will change. However,

Optics EXPRESS

as the length of FP cavity (W_1) varies, the changes in ϕ_r are actually rather subtle for the B-mode C_{spp}, and there is a tendency to continue to maintain the resonance order (m = 3) at the resonant wavelength of B mode. According to Eq. (5), we can predict that the resonant wavenumber (β) will increase due to the decrease of W_1, and the peak frequency of the B mode will shift toward the short wave direction. With the help of this theory, we change the width ratios of W_1 and W_2 with the fixed period length of P = 2 μm, and finally obtain the coupling spectral information of the A mode and the B mode, as shown in Fig. 6(a). As the ratio of W_2/W_1 progresses from small to large, the two modes exhibit a single coupling peak in the early stage and then gradually separate. Because of the stability of the A mode, the resonance wavelength λ_s is basically in a fixed position after separation, while the B mode has a significant blue shift wavelength and with intensity changes. When the material properties satisfy $\varepsilon_m\varepsilon_d<1, |\varepsilon_m|>>|\varepsilon_d|$, we found that the secondary harmonic resonance frequency of Wood anomalies (WA(2)) in the critical position of the transmission band gap will approach and be slightly higher than the peak frequency of the A mode. According to the research of Christ et al., the WAs appear when the light field of Bragg harmonics changes from evanescent to radiative in a substrate layer [53], and the periodic metal-dielectric nanostructure exhibits an extreme value of the transmittance. Through the study of the dispersion relation as $k_{W-R} = k_0\sqrt{\varepsilon_d}$ [52,53], we found that the working frequency of WA is indeed at the minimum position of the transmission spectrum, as shown in Fig. 6(a). This means that WA can effectively and sharply reduce the spectral energy, decreasing the line width and steepening the waveform. At the same time the photon energy of the S_{spp} resonance of the composite grating structure is 0.85 eV, which corresponds to the frequency of the second-order harmonic SPs(2) matched by the Bragg harmonic and SPs resonance. In fact this given frequency of 0.85 eV is also the edge of Brillouin zone. When the wavenumber spectrum of the SPs passes through this frequency point, an energy band gap will be generated [7], resulting in a significant decrease in transmittance. This also effectively suppresses the transmission line width. Naturally, we speculate that the band gap formed by the separation of the A mode and the B mode is the product of the two theories. Therefore, the physical origin of ultra-narrow line width is a combination of the transmission forbidden band gap and WA anomalous resonance.

Optics EXPRESS

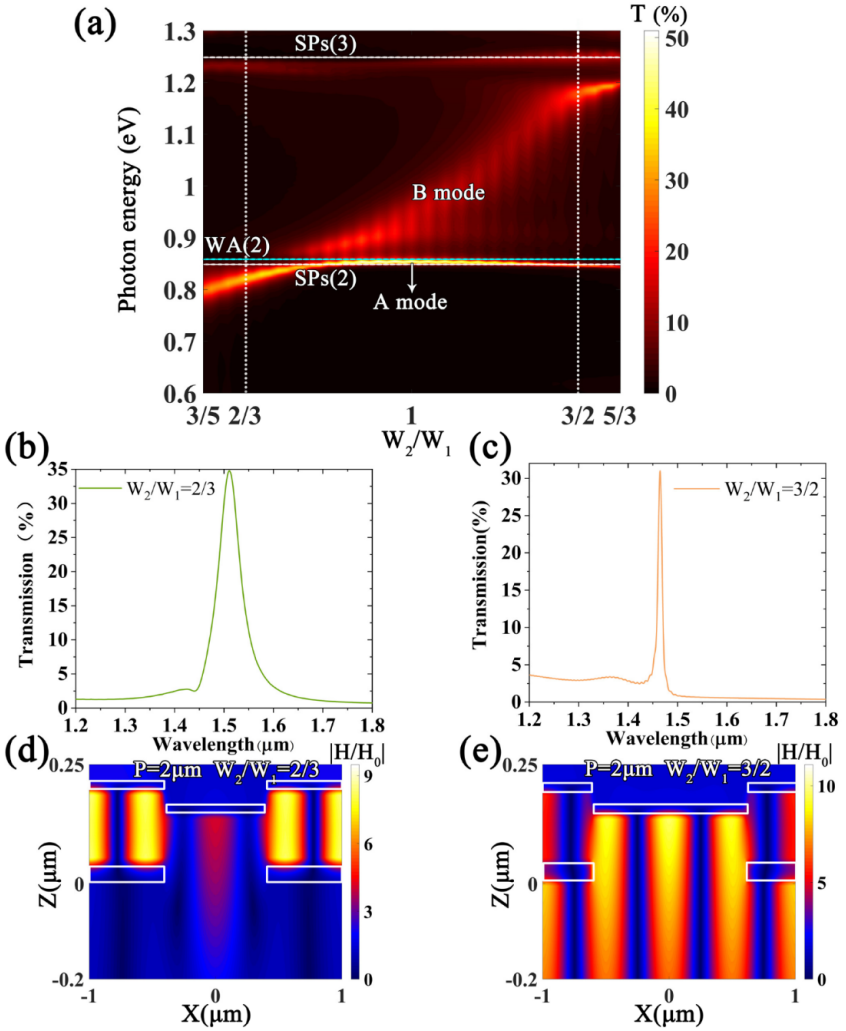

Fig. 6. (a) The transmission behavior of the designed microstructure is significantly modulated by the ratio of w2/w1 and frequency. (b) and (c) The transmission spectra with the ratio of W_2/W_1 = 2/3 and 3/2, respectively. (d) and (e) The relative magnetic field distributions under the conditions of W_2/W_1 = 2/3 and 3/2, respectively. The color bars stand for the normalized magnetic field intensity.

According to these discussions, for the purpose of obtaining a narrow-band single transmission peak in the near-infrared regime, we can provide two methods to realize the redistribution of energy forms, transform the main resonance mode, further modulate the line width and eliminate the side peaks. In the first method, when the ratio W_2/W_1 is 2/3, the simulated transmission spectrum shown in Fig. 6(b) is in the critical state of coupled resonance dominated by the B mode. At this time, there is only one peak formed in the working band. In the other method, when the ratio is 3/2, the main resonance position of the B mode moves far enough, so that there is an extremely narrow transmission peak as shown in Fig. 6(c) dominated by the A mode.

Optics EXPRESS

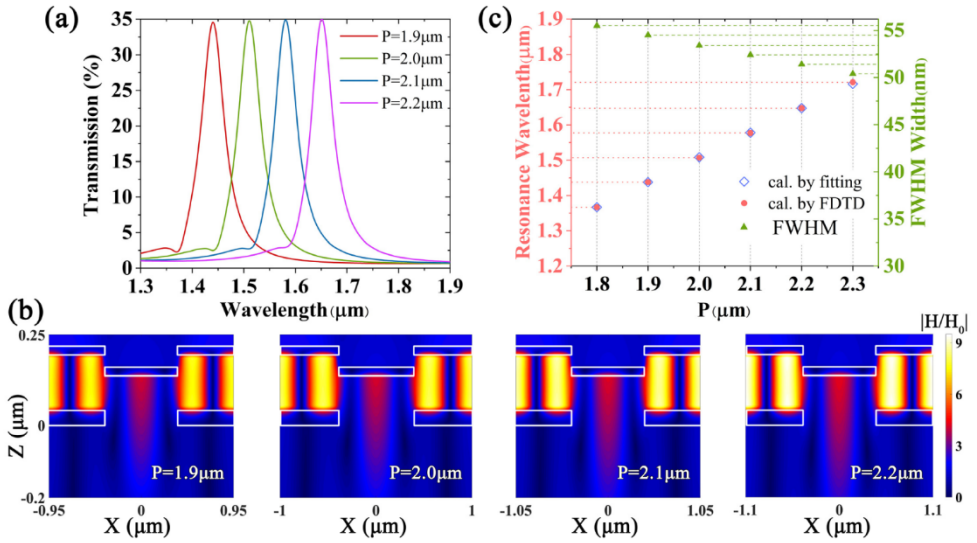

Fig. 7. (a) The dependence of transmission on the P of the compound-grating microstructure with the ratio of W_2/W_1 = 2/3. (b) The relative magnetic-field intensity distributions with different P's ranging from 1.9 μm to 2.2 μm. The color bars stand for the normalized magnetic field intensity. (c) The relationship between the P and transmission peak wavelength obtained by FDTD and fitting method respectively, and the corresponding FWHM values are also exhibited.

In the first case, the influence of the B mode plays a core role. Plainly, the C_{spp} magnetic resonance main order is m = 3 in the MIM cavity, and the light field energy is mainly confined in the dielectric cavity as shown in Fig. 6(d). The corresponding propagation wave vector value is $\beta = 7.02*10^6 + 1.70*10^4 i$ calculated from Eq. (4). The spilled energy passes through the end faces between MIM and MI to the Au-SiO_2 interface of the MI grating, and the provided wave vector increment excites SPP to form a transmission with an intensity of 34.8%. As mentioned above, C_{spp} is relatively weak in response to wavelength changes during the course of the order conversion, making the line width wider than the S_{spp} leading mode, but the FWHM width is 53.4 nm, which is a satisfactory scale. We further found that when maintaining the ratio of W_2/W_1 = 2/3, the change in P will modulate the resonance peak. Figure 7(a) displays the transmission distributions of the microstructure with P's ranging from 1.9 μm to 2.2 μm. These spectral curves show the stable and similar waveforms with a same resonant order m = 3 in MIM cavity observed from Fig. 7(b), and provide relatively ideal transmission and line width. With the continuous increase of the structural period the ability to localize the field of the compound gratings is strengthened, and the FWHM as shown in Fig. 7(c) is gradually reduced. To effectively predict the resonant wavelength of the C_{spp} mode using a mathematical model, we propose the concept of the effective refractive index n_{eff} formed as $n_{eff} = \beta/k_0$ of the MIM F-P cavity [44,46]. Naturally, under the precondition of W_2/W_1 = 2/3, the resonance wavelengths λ_r can be expressed by Eq. (6):

$$\lambda_r = \frac{6}{5} n_{eff} P / (m - \phi_r / 2\pi) \tag{6}$$

Undoubtedly, as long as we know the trend of n_{eff} and $\phi_r/2\pi$, we can quickly solve for the λ_r when the main order of resonance is definite (m = 3). First, taking the two transmission relationships obtained by periodic scanning shown in Fig. 7(a) as an example, we get the exact values of n_{eff} (β/k_0) and $\phi_r/2\pi$ when P = 1.9 μm (1.69 and 0.33) and P = 2.2 μm (1.68 and 0.31) from Eqs. (4) and (5) respectively. On the basis of this theory we can obtain other phase shifts $\phi_r/2\pi$ and n_{eff} values by linear fitting, and then calculate all resonant wavelengths

Optics EXPRESS

λ_r using Eq. (6) in the desired working band. To prove the rationality of the fitting method, we have scanned a wider range of periodic variation by FDTD. The relationship between the simulated peak position and the corresponding λ_r acquired by fitting the solution is also illustrated in Fig. 7(c). It is clear that the results calculated by the two methods are in good agreement, although the tiny separation is caused by the model to improve of n_{eff} and phase shift $\phi_r/2\pi$. The positive correlation between P and λ_r represented by Eq. (6) can explain the linear change and red shift phenomenon of the transmission spectrum. Therefore, in a reasonable band, this fitting calculation is a convenient and fast way to obtain the peak solution of the relevant model, by which we can avoid the large number of redundant simulations.

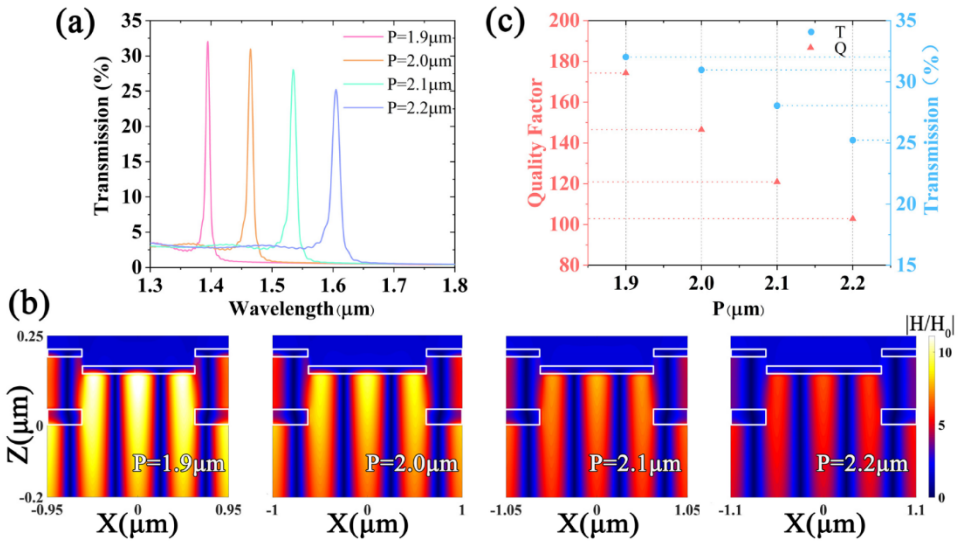

Fig. 8. (a) The dependence of transmission on the P of the compound-grating microstructure with the ratio of W_2/W_1 = 3/2. (b) The relative magnetic-field intensity distributions with different P's ranging from 1.9 μm to 2.2 μm. The color bars stand for the normalized magnetic field intensity. (c) The corresponding values for Q and transmittance in different P.

For the other case, the B mode is sufficiently far apart from the A mode. Clearly, as seen in Fig. 6(e) the field distribution indicates that the energy ratio of C_{spp} is significantly reduced, and S_{spp} plays a dominant role when the two modes are coupled. As a result, the transmission line width is further reduced to 10 nm as shown in Fig. 6(c), and the peak wavelength also moved to 1.465 μm, which is closer to the above analytical solution of 1.462 μm. Additionally, the side peak influence originating from C_{spp} on the transmission spectrum is obviously weakened. When the structure period is tuned with a constant ratio of W_2/W_1 = 3/2, not only the transmission peak wavelength can be modulated, but also it keeps a very narrow single-peak waveform, as shown in Fig. 8(a). As expected, the field distributions in Fig. 8(b) showing the different periodic structures at the resonant wavelength are similar, and the corresponding resonant main orders are the same. This is the result of the match between the Bragg coupling condition and the SPs wavenumber to form S_{spp}, and their resonant wavelengths are also consistent with the calculated results from Eq. (3). Spectral information such as the transmittance and the quality factor of each are illustrated in Fig. 8(c). When the P is 1.9 um, the transmission line width is only 8 nm, and the Q value is as high as 174.3. Ideal narrow line width, good transmittance, regular grating structure, weak side peak, miniaturization, and modular operating resonance wavelength indicate that our proposed structure has great potential applications for high resolution filters.

Optics EXPRESS

Finally, we shortly discuss the structure fabrication. It is a challenge to fabricate this structure because the suggested structure size is around 1 μm, close to the fabrication limit of traditional lithography process. We recommend that the bottom Au grating be fabricated firstly by using the lift-off lithography process, and subsequently SiO_2 and Au films be deposited through magnetron sputtering or thermal evaporation. Since the optical properties of this structure are sensitive to the structure parameters, a fabrication method with a higher precision such as laser direct writing and e-beam lithography is required. Besides lithography, the film fabrication with less oblique angle deposition is suggested to avoid sidewall deposition.

4. Conclusion

In summary, we have displayed a promising plasmonic composite grating array that provides two propagation-type SPPs mode coupling in the near-infrared region of 1.4-1.7 μm. The sharp transmission peak is attributed to the Fano-like resonance formed by the coupling between S_{spp} and C_{spp}, and the narrow line width is originated from a combination of energy band gap and WA resonance suppression. By adjusting the thickness H of the dielectric layer, the excitation mode of the MIM cavity significantly enhances out-of-band rejection. In addition, we have provided a method of changing the ratio of the widths of the two gratings, which not only eliminates the influence of the side peaks, but also realizes the linear modulation of the resonant wavelength and the control of the line width (the level of 10 nm and 50 nm). A transmission spectrum with a FWHM of only 8 nm and Q value of up to 174.3 was obtained. This composite grating structure effectively solves the problem of high transmission and narrow line width of plasmonic filters, and its characteristics are also beneficial when integrating with the photodetector, and have great application prospects in gas detection, biosensors, and multi-spectral imaging.

Funding

National Natural Science Foundation of China (61875193, 61675199 and 61705226); Science and Technology Innovation Project of Changchun City (19SS004); Science and Technology Innovation Project of Jilin Province (20190201126JC and 20190302082GX).

References

1. C. F. Guo, T. Sun, F. Cao, Q. Liu, and Z. Ren, "Metallic nanostructures for light trapping in energy-harvesting devices," Light Sci. Appl. **3**(4), e161 (2014).
2. M. L. Brongersma, "Introductory lecture: nanoplasmonics," Faraday Discuss. **178**, 9–36 (2015).
3. X. Liu, J. Gao, J. Gao, H. Yang, X. Wang, T. Wang, Z. Shen, Z. Liu, H. Liu, J. Zhang, Z. Li, Y. Wang, and Q. Li, "Microcavity electrodynamics of hybrid surface plasmon polariton modes in high-quality multilayer trench gratings," Light Sci. Appl. **7**(1), 14 (2018).
4. F. Pincella, K. Isozaki, and K. Miki, "A visible light-driven plasmonic photocatalyst," Light Sci. Appl. **3**(1), e133 (2014).
5. T. Allsop, R. Arif, R. Neal, K. Kalli, V. Kundrát, A. Rozhin, P. Culverhouse, and D. J. Webb, "Photonic gas sensors exploiting directly the optical properties of hybrid carbon nanotube localized surface plasmon structures," Light Sci. Appl. **5**(2), e16036 (2016).
6. W. L. Barnes, A. Dereux, and T. W. Ebbesen, "Surface plasmon subwavelength optics," Nature **424**(6950), 824–830 (2003).
7. C. Genet and T. W. Ebbesen, "Light in tiny holes," Nature **445**(7123), 39–46 (2007).
8. A. Kristensen, J. K. W. Yang, S. I. Bozhevolnyi, S. Link, P. Nordlander, N. J. Halas, and N. A. Mortensen, "Plasmonic colour generation," Nat. Rev. Mater. **2**(1), 16088 (2017).
9. Q. Li, Z. Li, X. Wang, T. Wang, H. Liu, H. Yang, Y. Gong, and J. Gao, "Structurally tunable plasmonic absorption bands in a self-assembled nano-hole array," Nanoscale **10**(40), 19117–19124 (2018).
10. E. Balaur, C. Sadatnajafi, S. S. Kou, J. Lin, and B. Abbey, "Continuously Tunable, Polarization Controlled, Colour Palette Produced from Nanoscale Plasmonic Pixels," Sci. Rep. **6**(1), 28062 (2016).
11. Y. Li, B. An, S. Jiang, J. Gao, Y. Chen, and S. Pan, "Plasmonic induced triple-band absorber for sensor application," Opt. Express **23**(13), 17607–17612 (2015).
12. W. L. Barnes, "Surface plasmon–polariton length scales: a route to sub-wavelength optics," J. Opt. A, Pure Appl. Opt. **8**(4), S87–S93 (2006).
13. Y. Zhao and A. Alù, "Manipulating light polarization with ultrathin plasmonic metasurfaces," Phys. Rev. B

Optics EXPRESS

Condens. Matter Mater. Phys. **84**(20), 205428 (2011).
14. T. Cao, S. Wang, and W. X. Jiang, "Tunable metamaterials using a topological insulator at near-infrared regim," RSC. Adv. **3**(42), 19474–19480 (2013).
15. Y.-H. Su, Y.-F. Ke, S.-L. Cai, and Q.-Y. Yao, "Surface plasmon resonance of layer-by-layer gold nanoparticles induced photoelectric current in environmentally-friendly plasmon-sensitized solar cell," Light Sci. Appl. **1**(6), e14 (2012).
16. K. Wu, T. Rindzevicius, M. S. Schmidt, K. B. Mogensen, S. Xiao, and A. Boisen, "Plasmon resonances of Ag capped Si nanopillars fabricated using mask-less lithography," Opt. Express **23**(10), 12965–12978 (2015).
17. Q. Min and R. Gordon, "Surface plasmon microcavity for resonant transmission through a slit in a gold film," Opt. Express **16**(13), 9708–9713 (2008).
18. A. E. Cetin, D. Etezadi, B. C. Galarreta, M. P. Busson, Y. Eksioglu, and H. Altug, "Plasmonic Nanohole Arrays on Robust Hybrid Substrate for Highly Sensitive Label-Free Biosensing," ACS Photonics **2**(8), 1167–1174 (2015).
19. B. Park, S. H. Yun, C. Y. Cho, Y. C. Kim, J. C. Shin, H. G. Jeon, Y. H. Huh, I. Hwang, K. Y. Baik, Y. I. Lee, H. S. Uhm, G. S. Cho, and E. H. Choi, "Surface plasmon excitation in semitransparent inverted polymer photovoltaic devices and their applications as label-free optical sensors," Light Sci. Appl. **3**(12), e222 (2014).
20. S. Wang, X.-Y. Wang, B. Li, H.-Z. Chen, Y.-L. Wang, L. Dai, R. F. Oulton, and R.-M. Ma, "Unusual scaling laws for plasmonic nanolasers beyond the diffraction limit," Nat. Commun. **8**(1), 1889 (2017).
21. C.-Z. Ning, "Semiconductor nanolasers and the size-energy-efficiency challenge: a review," Adv. Photonics. **1**(01), 014002 (2019).
22. R. F. Oulton, V. J. Sorger, D. A. Genov, D. F. P. Pile, and X. Zhang, "A hybrid plasmonic waveguide for subwavelength confinement and long-range propagation," Nat. Photonics **2**(8), 496–500 (2008).
23. L. Gao, L. Tang, F. Hu, R. Guo, X. Wang, and Z. Zhou, "Active metal strip hybrid plasmonic waveguide with low critical material gain," Opt. Express **20**(10), 11487–11495 (2012).
24. X.-C. Ma, Y. Dai, L. Yu, and B.-B. Huang, "Energy transfer in plasmonic photocatalytic composites," Light Sci. Appl. **5**(2), e16017 (2016).
25. A. K. Popov, "Nonlinear optics of backward waves and extraordinary features of plasmonic nonlinear-optical microdevices," Eur. Phys. J. D **58**(2), 263–274 (2010).
26. M. W. Klein, M. Wegener, N. Feth, and S. Linden, "Experiments on second- and third-harmonic generation from magnetic metamaterials," Opt. Express **15**(8), 5238–5247 (2007).
27. Y. Qu, Q. Li, H. Gong, K. Du, S. Bai, D. Zhao, H. Ye, and M. Qiu, "Spatially and Spectrally Resolved Narrowband Optical Absorber Based on 2D Grating Nanostructures on Metallic Films," Adv. Opt. Mater. **4**(3), 480–486 (2016).
28. J. Y. Lu, S. H. Nam, K. Wilke, A. Raza, Y. E. Lee, A. AlGhaferi, N. X. Fang, and T. Zhang, "Localized Surface Plasmon-Enhanced Ultrathin Film Broadband Nanoporous Absorbers," Adv. Opt. Mater. **4**(8), 1255–1264 (2016).
29. G. Dayal and S. A. Ramakrishna, "Design of highly absorbing metamaterials for infrared frequencies," Opt. Express **20**(16), 17503–17508 (2012).
30. J. Wang, C. Fan, P. Ding, J. He, Y. Cheng, W. Hu, G. Cai, E. Liang, and Q. Xue, "Tunable broad-band perfect absorber by exciting of multiple plasmon resonances at optical frequency," Opt. Express **20**(14), 14871–14878 (2012).
31. T. W. Ebbesen, H. J. Lezec, H. F. Ghaemi, T. Thio, and P. A. Wolff, "Extraordinary optical transmission through sub-wavelength hole arrays," Nature **391**(6668), 667–669 (1998).
32. J. B. Khurgin, "How to deal with the loss in plasmonics and metamaterials," Nat. Nanotechnol. **10**(1), 2–6 (2015).
33. D. K. Gramotnev and S. I. Bozhevolnyi, "Plasmonics beyond the diffraction limit," Nat. Photonics **4**(2), 83–91 (2010).
34. Q. Chen and D. R. S. Cumming, "High transmission and low color cross-talk plasmonic color filters using triangular-lattice hole arrays in aluminum films," Opt. Express **18**(13), 14056–14062 (2010).
35. T. Xu, Y.-K. Wu, X. Luo, and L. J. Guo, "Plasmonic nanoresonators for high-resolution colour filtering and spectral imaging," Nat. Commun. **1**(1), 59 (2010).
36. Y. D. Shah, J. Grant, D. Hao, M. Kenney, V. Pusino, and D. R. S. Cumming, "Ultra-narrow Line Width Polarization-Insensitive Filter Using a Symmetry-Breaking Selective Plasmonic Metasurface," ACS Photonics **5**(2), 663–669 (2018).
37. Y. S. Do, J. H. Park, B. Y. Hwang, S.-M. Lee, B.-K. Ju, and K. C. Choi, "Plasmonic Color Filter and its Fabrication for Large-Area Applications," Adv. Opt. Mater. **1**(2), 133–138 (2013).
38. I. J. H. McCrindle, J. P. Grant, L. C. P. Gouveia, and D. R. S. Cumming, "Infrared plasmonic filters integrated with an optical and terahertz multi-spectral material," Phys. Status Solidi., A Appl. Mater. Sci. **212**(8), 1625–1633 (2015).
39. B. Lee, S. Kim, H. Kim, and Y. Lim, "The use of plasmonics in light beaming and focusing," Prog. Quantum Electron. **34**(2), 47–87 (2010).
40. Z. Liao, Y. Luo, A. I. Fernández-Domínguez, X. Shen, S. A. Maier, and T. J. Cui, "High-order localized spoof surface plasmon resonances and experimental verifications," Sci. Rep. **5**(1), 9590 (2015).

Optics EXPRESS

41. J. Chen, P. Wang, Z. M. Zhang, Y. Lu, and H. Ming, "Coupling between gap plasmon polariton and magnetic polariton in a metallic-dielectric multilayer structure," Phys. Rev. E Stat. Nonlin. Soft Matter Phys. **84**(2 Pt 2), 026603 (2011).
42. Q. Li, Z. Li, H. Yang, H. Liu, X. Wang, J. Gao, and J. Zhao, "Novel aluminum plasmonic absorber enhanced by extraordinary optical transmission," Opt. Express **24**(22), 25885–25893 (2016).
43. E. D. Palik, *Handbook of Optical Constants of Solids* (Academic, 1985).
44. S. Shu and Y. Y. Li, "Triple-layer Fabry-Perot/SPP aluminum absorber in the visible and near-infrared region," Opt. Lett. **40**(6), 934–937 (2015).
45. P. Fan, Z. Yu, S. Fan, and M. L. Brongersma, "Optical Fano resonance of an individual semiconductor nanostructure," Nat. Mater. **13**(5), 471–475 (2014).
46. B. Luk'yanchuk, N. I. Zheludev, S. A. Maier, N. J. Halas, P. Nordlander, H. Giessen, and C. T. Chong, "The Fano resonance in plasmonic nanostructures and metamaterials," Nat. Mater. **9**(9), 707–715 (2010).
47. F. Hu, H. Yi, and Z. Zhou, "Band-pass plasmonic slot filter with band selection and spectrally splitting capabilities," Opt. Express **19**(6), 4848–4855 (2011).
48. X. L. Hu, L. B. Sun, B. Zeng, L. S. Wang, Z. G. Yu, S. A. Bai, S. M. Yang, L. X. Zhao, Q. Li, M. Qiu, R. Z. Tai, H. J. Fecht, J. Z. Jiang, and D. X. Zhang, "Polarization-independent plasmonic subtractive color filtering in ultrathin Ag nanodisks with high transmission," Appl. Opt. **55**(1), 148–152 (2016).
49. X. Liu, J. Gao, H. Yang, X. Wang, S. Tian, and C. Guo, "Hybrid Plasmonic Modes in Multilayer Trench Grating Structures," Adv. Opt. Mater. **5**(22), 1700496 (2017).
50. M. Bora, E. M. Behymer, D. A. Dehlinger, J. A. Britten, C. C. Larson, A. S. P. Chang, K. Munechika, H. T. Nguyen, and T. C. Bond, "Plasmonic black metals in resonant nanocavities," Appl. Phys. Lett. **102**(25), 251105 (2013).
51. S.-H. Chang and Y.-L. Su, "Mapping of transmission spectrum between plasmonic and nonplasmonic single slits. I: resonant transmission," J. Opt. Soc. Am. B **32**(1), 38–44 (2015).
52. G. Li, Y. Shen, G. Xiao, and C. Jin, "Double-layered metal grating for high-performance refractive index sensing," Opt. Express **23**(7), 8995–9003 (2015).
53. A. Christ, T. Zentgraf, J. Kuhl, S. G. Tikhodeev, N. A. Gippius, and H. Giessen, "Optical properties of planar metallic photonic crystal structures: Experiment and theory," Phys. Rev. B Condens. Matter Mater. Phys. **70**(12), 125113 (2004).